

Article

Hydrogenolysis of Lignin and C–O Linkages Containing Lignin-Related Compounds over a Macroporous Silicalite-1 Array-Supported Ru-Ni Phosphide Composite

Bo Chen ^{1,2,*}, Zhi-Ze Cao ¹, Zhi-Jun Diao ^{3,*}, Liang-Qiu Huang ³, Si-Jia Zhao ³, Hong Yuan ¹ and Jia-Meng He ³¹ School of Chemical Engineering, Northwest University, Xi'an 710069, China² Xi'an Giant Biological Gene Technology Co., Ltd., Xi'an 710077, China³ College of Urban and Environment Science, Northwest University, Xi'an 710127, China

* Correspondence: bochen@nwu.edu.cn (B.C.); zjdiao@nwu.edu.cn (Z.-J.D.)

Abstract: Hydrogenolysis via targeted depolymerization of C–O linkages is a techno-economic beneficial process for converting lignin into highly valuable chemicals and clean fuels. In this work, a macroporous silicalite-1 (S-1) array-supported Ru-Ni metallic phosphide composite (Ru-Ni₁₂P₅/S-1₅) was prepared as a catalyst and hydrogenolysis activity under relative mild conditions was investigated using a series of compounds containing ether linkages as lignin-related model compounds. The Lewis acid sites originating from the unreduced Ru species and the macroporous geometry of S-1 significantly influenced hydrogenolysis activity and product selectivity. Analysis of the mechanism demonstrated that both the aryl ether and aliphatic ether linkages were directly hydrogenated over Ru-Ni₁₂P₅/S-1₅. 2D-HSQC-NMR spectroscopy demonstrated that the ether linkages of lignin were efficiently cleaved by Ru-Ni₁₂P₅/S-1₅. Furthermore, the obtained liquid hydrogenolysis products are high value-added chemicals used for pharmaceutical production and can be facilely tuned via the reaction conditions.

Keywords: hydrogenolysis; macroporous array; C–O linkages; lignin; model compounds



Citation: Chen, B.; Cao, Z.-Z.; Diao, Z.-J.; Huang, L.-Q.; Zhao, S.-J.; Yuan, H.; He, J.-M. Hydrogenolysis of Lignin and C–O Linkages Containing Lignin-Related Compounds over a Macroporous Silicalite-1 Array-Supported Ru-Ni Phosphide Composite. *Catalysts* **2022**, *12*, 1625. <https://doi.org/10.3390/catal12121625>

Academic Editor: Narendra Kumar

Received: 9 November 2022

Accepted: 9 December 2022

Published: 11 December 2022

Publisher's Note: MDPI stays neutral with regard to jurisdictional claims in published maps and institutional affiliations.



Copyright: © 2022 by the authors. Licensee MDPI, Basel, Switzerland. This article is an open access article distributed under the terms and conditions of the Creative Commons Attribution (CC BY) license (<https://creativecommons.org/licenses/by/4.0/>).

1. Introduction

The depletion of oil reserves and environmental issues relevant to the use of traditional fuels has prompted the manufacture of chemicals and fuels from renewable sources [1]. The conversion of lignocellulosic biomass into chemical raw materials is particularly significant to diminish dependence on traditional fuels [2].

Lignin, a conceivable lignocellulosic biomass for the production of aromatic chemicals and fuels [3,4], consists of phenylpropane-related structural units linked by bridge linkages [5]. However, more than 80% of bridge linkages are etheric, implying that the depolymerization of ether linkages is a critical step for a higher value-added exploitation of lignin. Notably, 4–O–5 bonds are highly stable due to the higher bond dissociation energy as compared to α -O–4 and β -O–4 linkages. Thus, the efficient cleavage of 4–O–5 bonds remains a significant challenge to the biorefinery industry. Usually, diphenyl ether is selected as a lignin-related probe compound to investigate potential catalysts for cleaving 4–O–5 linkages.

Hydrogenolysis via targeted depolymerization of C–O linkages is a techno-economic beneficial process for the conversion of lignin to highly valuable chemicals and clean fuels as compared to pyrolysis, oxidation degradation, and gasification [6,7].

Various hierarchically macroporous materials have been investigated as potential catalysts to enhance the diffusion of reactants and products in liquid-phase reactions and also reduce the distance among molecules to improve catalytic activity and selectivity [8,9]. The improved reactant-catalyst contact efficiency of three-dimensional ordered macroporous materials has enhanced the performance of gas phase-related reactions [10,11].

However, the use of macroporous materials as catalysts for macromolecular reactants, such as lignin and thermal extractions of coals, in liquid-phase reactions has been relatively limited. Recently, Luo et al. found that a hierarchical macro/mesoporous Ni/ASA-supported catalyst facilitated the transport and hydrodepolymerization of lignin, resulting in a yield of ca. 43 wt% for liquid hydrocarbons [12].

Transition metal phosphides are widely applied as catalysts for the hydrotreatment of bio-oils [13], whereas monometallic phosphides are typically used as catalysts under harsh reaction conditions, such as high temperatures and H₂ partial pressure [14,15]. The incorporation of noble-metal like Ru, one of the cheapest noble metals, can efficiently enhance the performance of transition metal phosphides and simultaneously moderate the reaction conditions [16–18]. However, the dominant disadvantage of metal-based catalysts is the inevitable deactivation due to carbon deposition and metal particles sintering [19–22]. It is reasonable to believe that catalysts with a macroporous structure should diminish transport limitations and possess better coke-resistant ability, and thus, could extend the catalysts lifetime [23].

In the present work, a macroporous silicalite-1 (S-1) array-supported Ru-Ni metallic phosphide composite (Ru-Ni₁₂P₅/S-1₅) was prepared and employed for the depolymerization of lignin and C–O linkages containing lignin-related compounds. The results demonstrated that the electron-enriched Ru^{δ+} species and the macroporous array-confined effect promoted the hydrogenolysis of C–O linkages and hydrodeoxygenation even under relative mild conditions, indicating that the geometry of the porous structure plays a pivotal role in macromolecule-related reactions. Macromolecular reactants can be efficiently captured using a fishing net-like macroporous array, and preferentially undergo hydrodeoxygenation/hydrogenation due to the higher concentration of active hydrogen species in the interior of the microporous. Moreover, the liquid hydrogenolysis products from lignin are important pharmaceutical precursors and can be obtained by facilely tuning the reaction conditions. Our present work indicates a feasible strategy for the production of high value-added chemicals from the lignin and thermal extractions of coals.

2. Results and Discussion

2.1. Characterization of the Catalysts

The particle size of the solid S-1 nanocubes was about 300 nm, as shown in Figure 1a. After three days of recrystallization, the shells of the nanocubes were punctuated with macropores of about 200 nm in diameter (Figure 1b). As the recrystallization time was extended to four days, the macroporous nanocubes formed short-range ordered aggregates (Figure 1c), which was attributed to continuous desilication and recrystallization during the alkali treatment process [24]. Moreover, as displayed in Figure 1d,e, a highly ordered macroporous array-like structure formed when the recrystallization time was prolonged to five days. TEM (Figure 1f) further confirmed that the macropores were hollow and interconnected. As compared to S-1, the macroporous array structure of S-1₅ allowed for macromolecule-related reactions in the liquid phase.

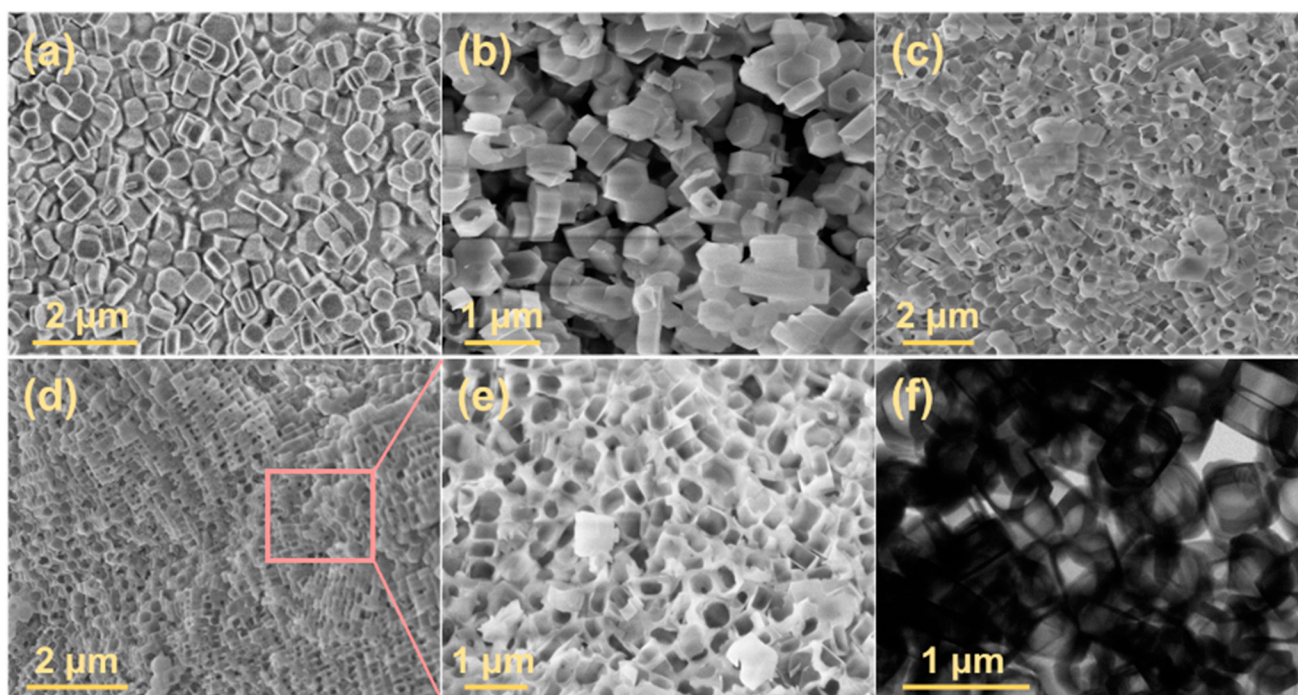


Figure 1. Scanning electron microscopy images of (a) S-1, (b) S-13, (c) S-14 and (d,e) S-15; and (f) TEM image of S-15.

As shown in Figures 2a and 3a, the Ni phosphide was successfully loaded into the interior cavity of the S-15 structure, as demonstrated by characteristic peaks of the Ni_{12}P_5 phase at $\sim 49.0^\circ$, 47.0° , and 38.4° (Figure 2b) [25]. However, Ru phosphide might exist in an amorphous form [26] due to the lack of signals of any feature peaks, and thus, was denoted as RuP_x . In addition, the X-ray diffraction patterns of Ru-Ni bimetallic phosphide ($\text{Ru-Ni}_{12}\text{P}_5$) closely resembles that of Ni_{12}P_5 , indicating that $\text{Ru-Ni}_{12}\text{P}_5$ is likely a composite of RuP_x and Ni_{12}P_5 . Due to the limitations of the incipient wetness impregnation method, P, Ni, and Ru were non-homogeneously distributed on the interior surface of the macropores of the S-15 structure, as displayed in Figure 3a–f. Moreover, the distinct distributions of Ni and Ru further revealed that $\text{Ru-Ni}_{12}\text{P}_5$ is a composite rather than solid solution.

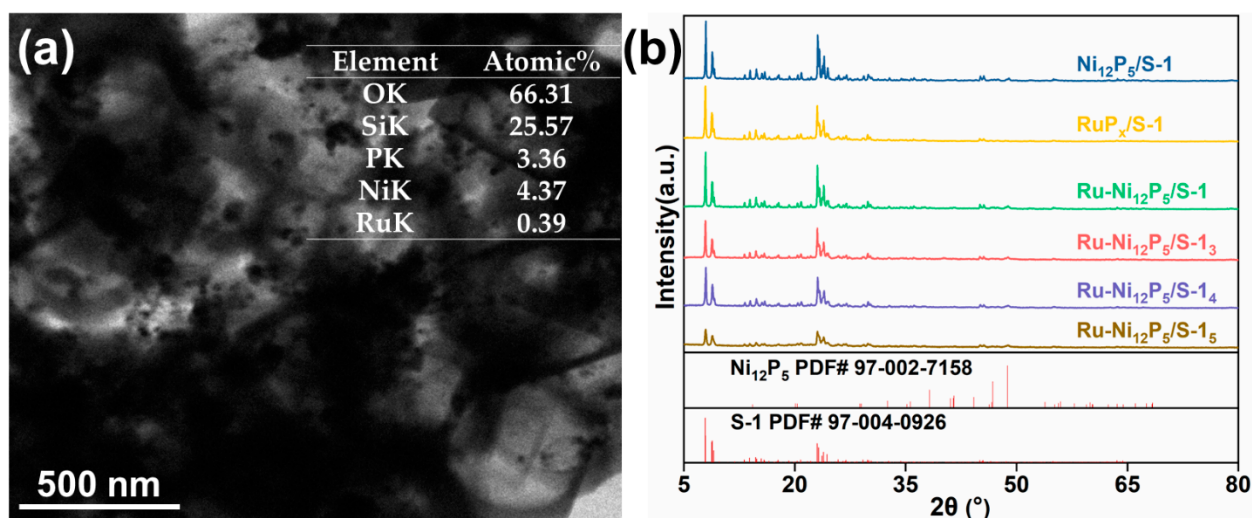


Figure 2. (a) TEM-EDS results of $\text{Ru-Ni}_{12}\text{P}_5/\text{S-15}$ and (b) XPD patterns of catalysts.

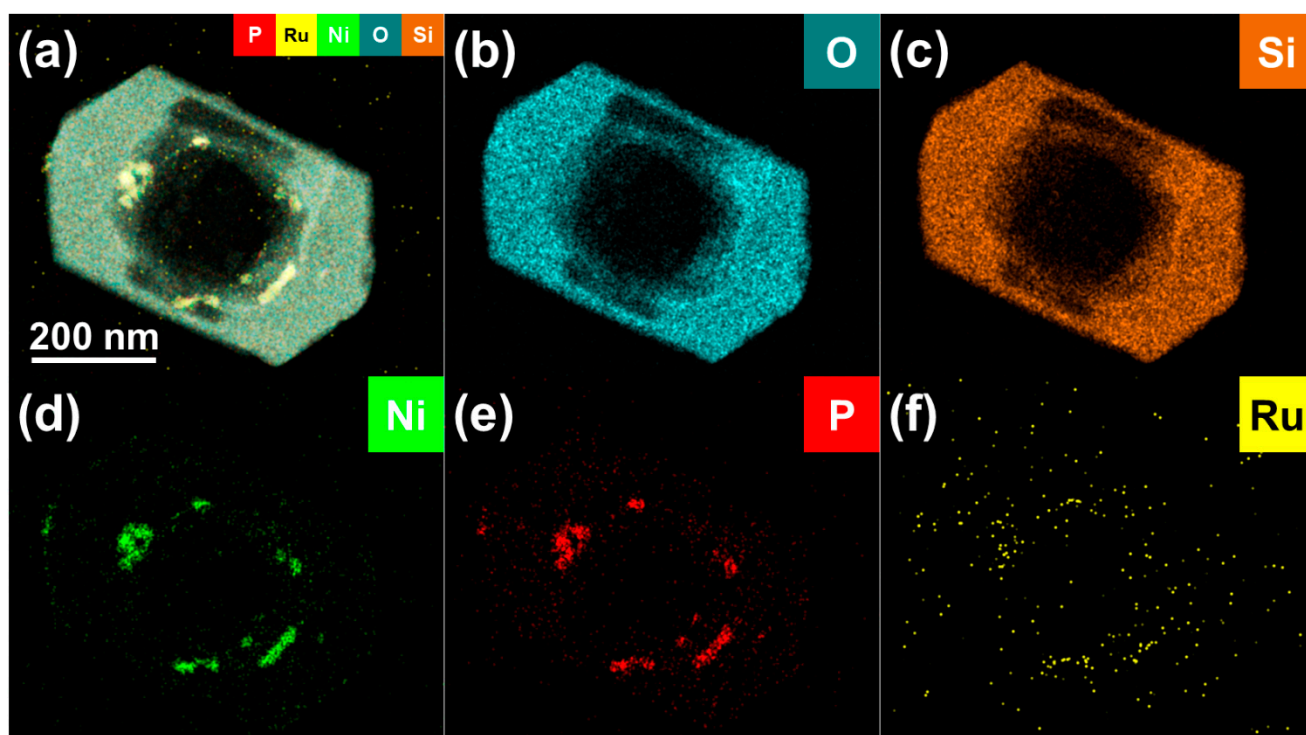


Figure 3. (a–f) TEM mapping of Ru-Ni₁₂P₅/S-1₅.

The surface chemical states of Ru, Ni, and P in Ru-Ni₁₂P₅/S-1₅ are presented in Figure 4. In the Ni₁₂P₅ phase, four apparent Ni (2p_{3/2}) peaks centered at 862.3, 858.5, 856.5 and 853.1 eV were assigned to satellite, Ni³⁺, Ni²⁺, and Ni^{δ+} species [27,28], respectively, as displayed in Figure 4a. Similar to amorphous RuP_x, two Ru (3p_{3/2}) peaks with binding energies of 466.1 and 462.6 eV, respectively, were attributed to Ru⁴⁺ and Ru^{δ+} species [29] (Figure 4b). Previous studies found that these metal species with a very small charge ($\delta \approx 0$) in metallic phosphides, especially the Ru^{δ+} species, facilitates hydrogen activation [26,30]. Notably, no apparent electron transfer between Ru and Ni species was detected in Ru-Ni metal phosphide, confirming that Ru-Ni₁₂P₅ is a composite.

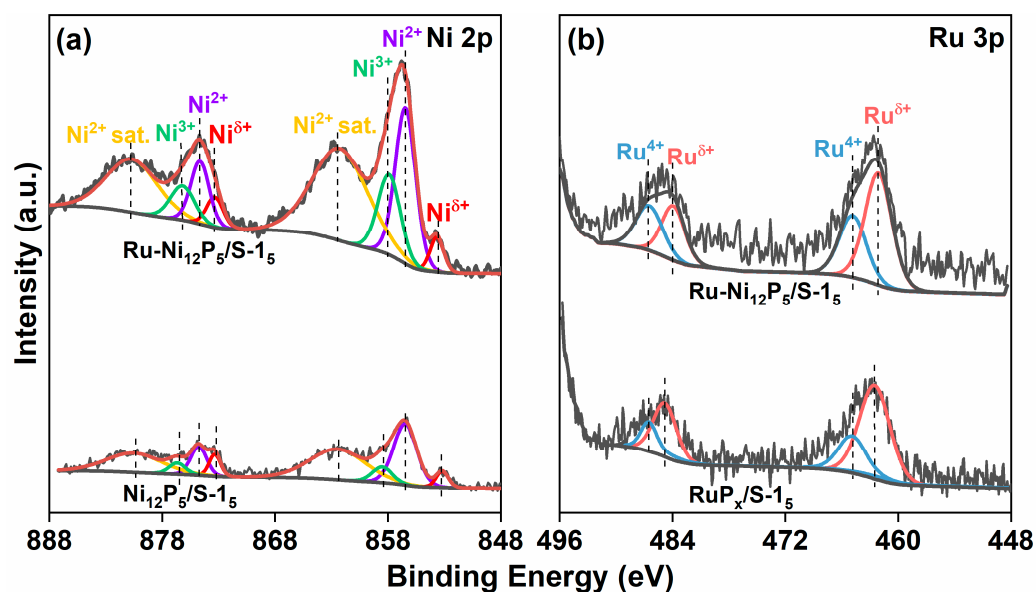


Figure 4. X-ray photoelectron spectrum of Ru-Ni₁₂P₅/S-1₅ in (a) Ni 2p and (b) Ru 3p regions.

According to the NH_3 -TPD results (shown in Figure 5), the acid properties of the catalysts are listed in Table 1. As displayed in Figure 5, only $\text{RuP}_x/\text{S-1}_5$ exhibits an apparent NH_3 desorption peak at $\sim 450^\circ\text{C}$ which might be attributed to Lewis acid sites originating from the unreduced Ru species [31]. Due to the low content of Ru, the NH_3 -TPD curve of $\text{Ru-Ni}_{12}\text{P}_5/\text{S-1}_5$ is closely similar to that of $\text{Ni}_{12}\text{P}_5/\text{S-1}_5$. However, the total acidity of $\text{Ru-Ni}_{12}\text{P}_5/\text{S-1}_5$ as a composite is much higher than those of monometallic phosphides, i.e., $\text{Ni}_{12}\text{P}_5/\text{S-1}_5$ and $\text{RuP}_x/\text{S-1}_5$.

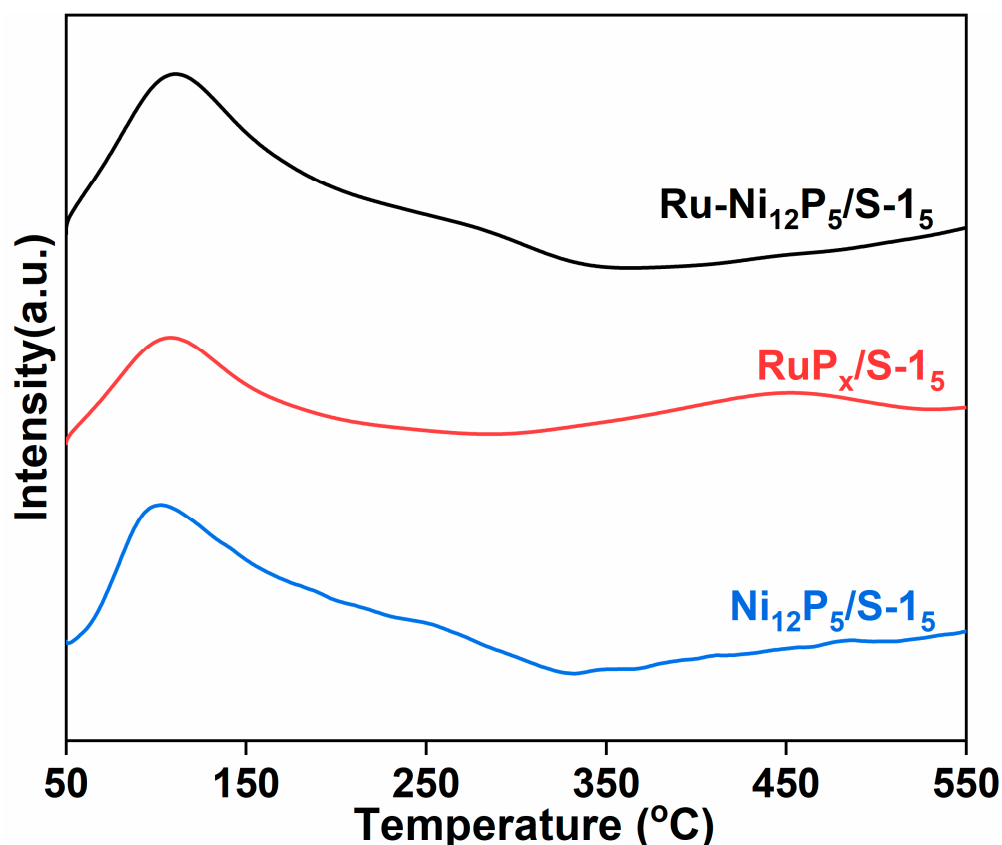


Figure 5. NH_3 -TPD profiles of the catalysts.

Table 1. Acid sites analysis by NH_3 -TPD.

Sample	$\text{Ni}_{12}\text{P}_5/\text{S-1}_5$	$\text{RuP}_x/\text{S-1}_5$	$\text{Ru-Ni}_{12}\text{P}_5/\text{S-1}_5$
NH_3 acidity/ $\text{mmol}\cdot\text{g}^{-1}$	0.19	0.13	0.25

2.2. Hydrogenolysis of Diphenyl Ether

2.2.1. Effect of a Porous Structure on Catalytic Performance

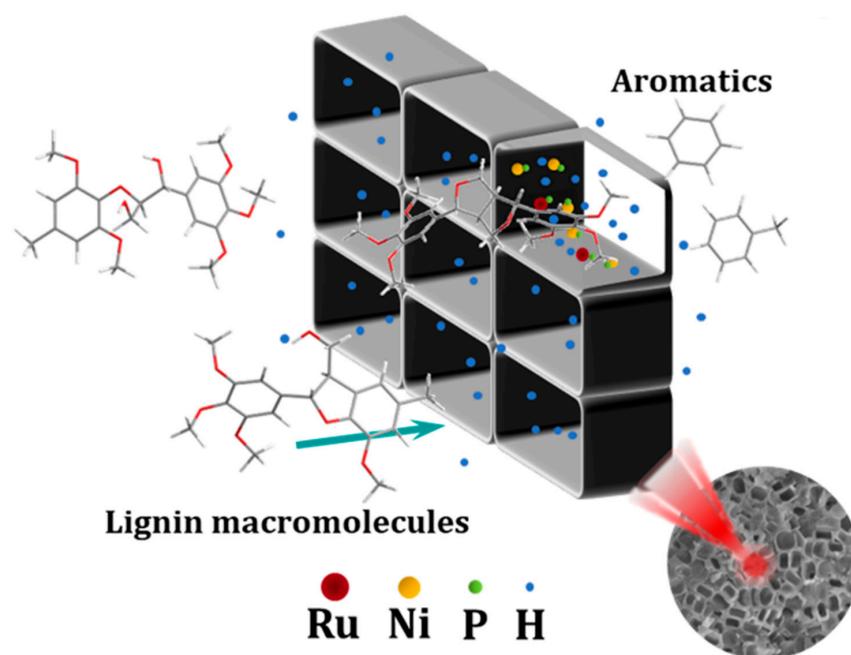
The activity of the catalyst $\text{Ni}_{12}\text{P}_5/\text{S-1}$ for depolymerization of diphenyl ether with hydrogenolysis conversion was negligible at only 0.5% (Table 2, entry 1). As compared to $\text{Ni}_{12}\text{P}_5/\text{S-1}$, the catalytic reactivity of $\text{RuP}_x/\text{S-1}$ for hydrogenolysis of diphenyl ether was much higher with a conversion rate of 66.5% (Table 2, entry 2). However, when employing $\text{Ru-Ni}_{12}\text{P}_5/\text{S-1}$ as a catalyst, the hydrogenolysis conversion rate and benzene yield were 94.7% and 40.5%, respectively (Table 2, entry 3). These results indicate that Lewis acid sites, i.e., unreduced Ru species (as illustrated by NH_3 -TPD results in Figure 5), play a pivotal role in the hydrogenolysis of C–O linkages.

Table 2. Hydrogenolysis of diphenyl ether over different catalysts.

Entry	Catalyst	Conv. (%)	Yield (%)				
							
1	Ni ₁₂ P ₅ /S-1	0.5	0.2	-	-	-	-
2	RuP _x /S-1	66.5	20.4	1.3	17.4	0.6	1.2
3	Ru-Ni ₁₂ P ₅ /S-1 ^a	94.7	40.5	3.6	21.8	3.1	2.7
4	Ru-Ni ₁₂ P ₅ /S-1 ₃	97.4	45.3	7.0	12.6	2.6	1.7
5	Ru-Ni ₁₂ P ₅ /S-1 ₄	97.3	50.2	8.0	3.1	3.1	1.9
6	Ru-Ni ₁₂ P ₅ /S-1 ₅ ^b	99.4	57.2	13.8	1.3	0.3	0.2

^a S_{BET}(S-1) = 482 m²·g⁻¹ [24]; ^b S_{BET}(S-1₅) = 389 m²·g⁻¹ [24].

Importantly, the macroporous structure of a support also has a significant influence on hydrogenolysis (Table 2, entries 3–6). A previous study illustrated that catalysts with larger pores favor the hydrodepolymerization of kraft lignin in bio-oil production [32]. The use of the highly ordered macroporous array S-1₅ as a support afforded the maximum hydrogenolysis conversion rate and benzene yield of 99.4% and 57.2%, respectively (Table 2, entry 6) and resulted in a minimum yield of oxygen-containing products, including phenol, cyclohexanol, and cyclohexanone. The interconnected macroporous array with pore diameters of ~200 nm promotes mass transport [33–35] and acts as a “fishing net” that captures lignin macromolecules in the liquid phase. Subsequently, the captured lignin macromolecules moved into the interior of the macropores and were hydrogenolyzed into smaller molecular products. Notably, even though S-1 has a larger total surface area than S-1₅, the corresponding supported Ru-Ni₁₂P₅ exhibited distinct reactivity for the catalytic hydrogenolysis of diphenyl ether (Table 2, entries 3 and 6). This phenomenon is supposed to be related to pore confined-like effect, as illustrated in Figure 6. It can be seen that the concentration of active hydrogen species in the interior of the macroporous array S-1₅ was greater than that on the surface of S-1, which might account for the preeminent hydrodeoxygenation selectivity of Ru-Ni₁₂P₅/S-1₅. Moreover, the highly ordered macroporous array S-1₅ also facilitated hydrogenation with a maximum cyclohexane yield of 13.8%.

**Figure 6.** Schematic illustration of hydrogenolysis reactivity under a pore confined-like effect.

2.2.2. Effect of H₂ Partial Pressure on Catalytic Performance

The initial H₂ partial pressure had a significant effect on the hydrogenolysis of performance (Figure 7). The hydrogenolysis conversion of diphenyl ether was merely 16.9% under an initial H₂ partial pressure of 0.2 MPa, but increased to 99.2% at 0.6 MPa, while the benzene yield achieved a maximum value of 57.2%. However, the phenol and cyclohexanol yields sharply decreased to 1.3%, while the cyclohexane yield increased to 13.8%. As the initial partial pressure was continuously increased to 1.0 MPa, the hydrogenolysis conversion rate and cyclohexane yield remained nearly unchanged, whereas the benzene yield dropped dramatically to 34.5%, likely due to subsequent hydrodeacyclization of benzene-derived hydrogenation products to afford paraffin (C1-C6) [36], which is less soluble in the aqueous phase. These results demonstrate that increasing the H₂ partial pressure did not accelerate the hydrogenolysis reaction [26].

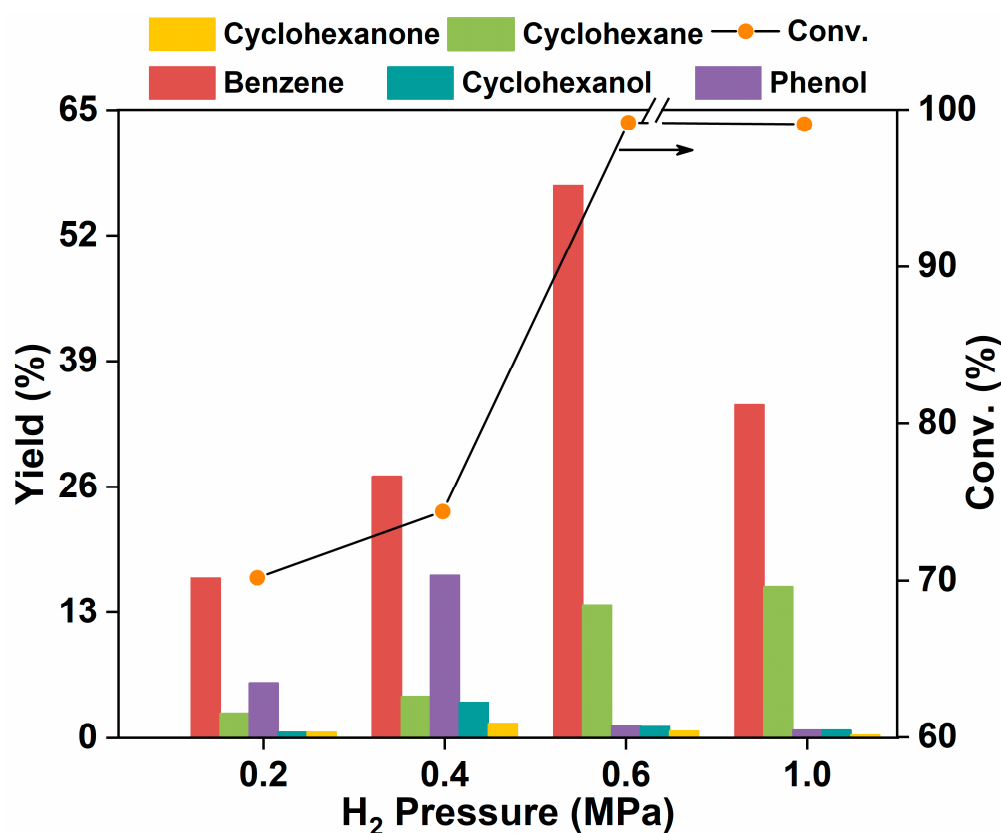


Figure 7. Effects of initial H₂ partial pressure on the hydrogenolysis of diphenyl ether over Ru-Ni₁₂P₅/S-1₅.

2.3. Reaction Mechanism

To obtain further insights into the hydrogenolysis mechanism, 3-phenoxytoluene was selected as a probe compound. As shown in Figure 8, metal phosphides, as a bifunctional catalyst, have excellent potential for cleaving C–O linkages [37,38]. Over metal phosphides, H₂ can be heterolytically split into H[−] and H⁺ species [39], which become subsequently trapped by Lewis acid sites (e.g., Ru^{δ+} and Ni^{δ+}) [40,41], while the negatively charged P and PO species form Brønsted sites (PO–H) [40,42,43] are notably much less active than Lewis acid sites in hydrogenolysis and hydrodeoxygenation [40,44], indicating that H[−] species are essential for C–O cleavage. Essentially, the 4–O–5 linkage is not easily cleaved, even in thermal strong acid solution [45]. However, due to the complexity of the chemical reaction, there is presently no clear atomistic description for the hydrogenolysis of C–O linkages on metal phosphides. Even so, we centered our endeavors on the reaction pathways that were

consistent with the catalytic experiments, while not denying the existence of other complex reaction pathways.

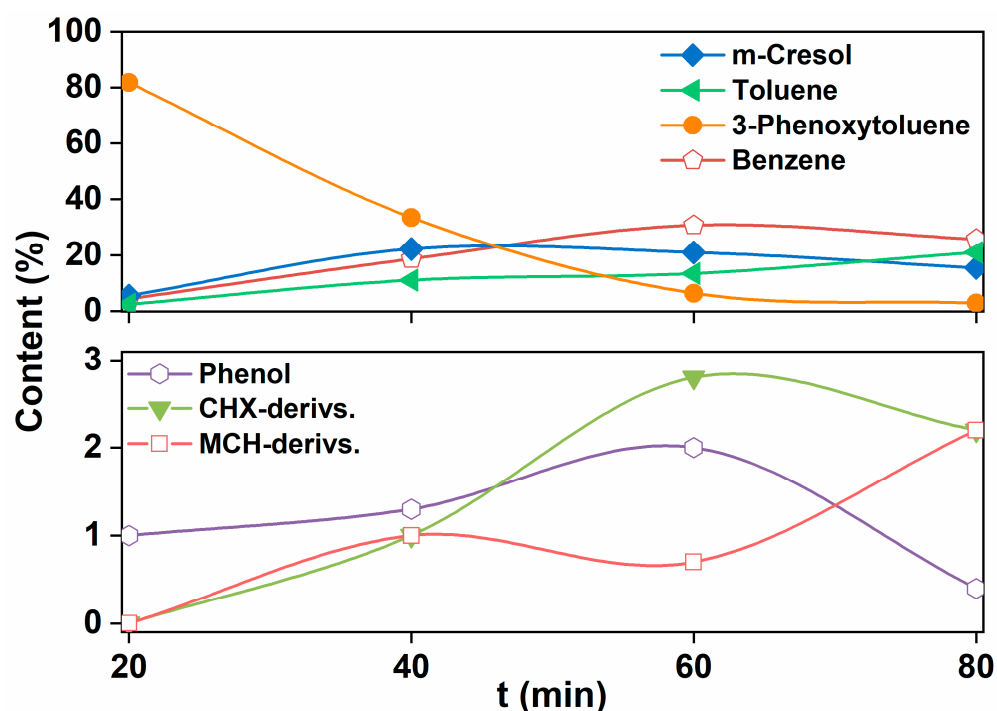
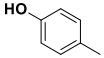
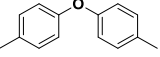
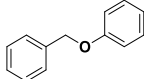
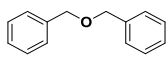


Figure 8. Time profiles of hydrogenolysis of 3-phenoxytoluene over Ru-Ni₁₂P₅/S-1₅. CHX-derivs: Cyclohexene-derivatives, including cyclohexane, cyclohexanol, and cyclohexanone; MCH-derivs: methylcyclohexane-derivatives, including methylcyclohexane, 3-methylcyclohexanol and 3-methylcyclohexanone.

Accordingly, possible reaction pathways for the catalytic hydrogenolysis of 3-phenoxytoluene over Ru-Ni₁₂P₅/S-1₅ are proposed in Scheme 1. As demonstrated by the time profile of the product evolution presented in Figure 8, during hydrogenolysis, route 2 is thermodynamically favorable as compared to route 1. In route 2, 3-phenoxytoluene, an unsymmetrical diaryl ether, is preferentially initially hydrogenolyzed by H⁻ attacking substituted aromatic carbon atom at the electron-deficient benzene-ring side with Lewis sites (e.g., unreduced Ru species) assistance [46], resulting in the generation of intermediate im22 and benzene via intermediate im2. Subsequently, intermediate im22 abstracts H⁺ from Brønsted sites or other H-donor, such as H₂O, leading to the formation of *m*-cresol. As a dominant intermediate product, *m*-cresol was sequentially dehydroxylated in the formation of toluene via the thermodynamically favorable intermediate im23, which resulted from H⁻ attacking hydroxyl-substituted aromatic carbon atom. Concomitantly, a slight amount of *m*-cresol was hydrogenated to 3-methylcyclohexanol as a by-product.

Table 3. Hydrogenolysis of different model compounds over Ru-Ni₁₂P₅/S-1₅.

Entry	Substrate	Conv. (%)	Yield (%)						
									
1		92.3	40.8	12.6	-	-	-	-	-
2		98.9	-	-	-	35.8	37.6	5.4	0.8
3		100.0	67.8	-	-	3.0	-	-	-
4		100.0	42.3	-	1.6	20.3	2.3	1.5	1.3
5		99.6	88.0	-	-	9.8	-	-	-

2.5. Catalytic Hydrogenolysis of Lignin by Ru-Ni₁₂P₅/S-1₅

2D-HSQC-NMR spectroscopy was employed to investigate changes to the C–O linkages of lignin and any corresponding residue [48–50]. As displayed in Figure 9a, the strong signals of –OCH₃ ($\delta_C/\delta_H = (3.7\text{--}4.0)/(53.2\text{--}55.8)$ ppm) illustrate that lignin contains large amounts of methoxyaryl moieties. Moreover, obvious correlations among C_α–H_α, C_β–H_β, and C_γ–H_γ ($\delta_C/\delta_H = 61.3/3.5, (77.1\text{--}79.2)/(4.4\text{--}4.5),$ and $(58.0\text{--}60.0)/3.9$ ppm, respectively) demonstrate that A is the predominant structural unit of lignin rather than B and C. After three hours of hydrogenolysis, the signals of A, B, and C had disappeared and that of the methoxyl group became weaker, as shown in Figure 9b. After six hours of hydrogenolysis, the signals of the methoxyl groups finally vanished, indicating that the C–O linkages of lignin had been completely cleaved (Figure 9c).

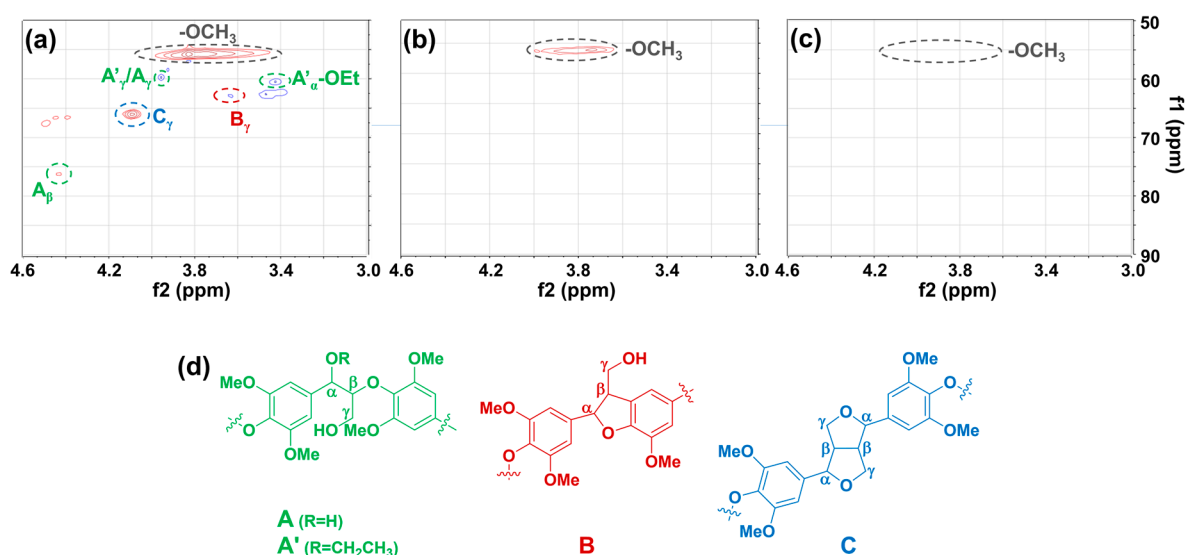
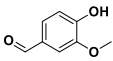
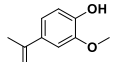
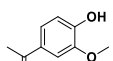
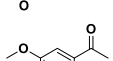
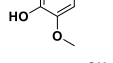
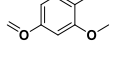
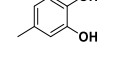
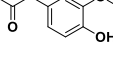
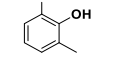
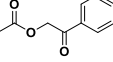


Figure 9. 2D-HSQC-NMR spectroscopy of C–O linkages for (a) fresh dealkaline lignin and (b) after three hours and (c) six hours of hydrogenolysis; (d) representative structures of ether linkages for lignin.

The hydrogenolysis products of lignin, as determined by HPLC-TQMS, are listed in Table 4. Notably, the yields of almost all products had increased over an initial six hours, revealing that cleavage of the ether linkages of lignin was incomplete for the initial

three hours over Ru-Ni₁₂P₅/S-15, in accordance with the results exhibited in Figure 9. When further prolonging the hydrogenolysis time to 12 h, the yields of all methoxyl-containing products remarkably decreased to zero, whereas those of 4-methylcatechol and 3-methylcatechol markedly increased to 103.6 and 25.3 µg, respectively. These results suggest that polyphenolics might be produced by hydrogenolysis of the methoxyl-containing moieties of lignin. Moreover, these findings demonstrate that different higher value-added compounds, such as vanillin and 4-methylcatechol, can be obtained by facilely tuning the reaction conditions. Vanillin is an important pharmaceutical intermediate with antiepileptic and antibacterial activities that is used for the synthesis of drugs for treatment of hypertension and heart disease [51]. Acting as a hapten and an antimicrobial as well as an antioxidant, 4-methylcatechol has a strong antiplatelet effect that is useful for the treatment of diabetic neuropathy and tumors [52,53].

Table 4. The predominant products from the hydrogenolysis of lignin.

Products	Structure	Yield (µg)		
		3 h	6 h	12 h
Vanillin		94.9	103.2	0.0
Isoeugenol		19.3	32.1	0.0
Acetovanillone		19.5	27.0	2.9
Acetosyringone		0.2	0.1	0.0
4-Vinylguaiacol		12.1	9.4	8.2
4-Methylcatechol		12.0	13.1	103.6
4-Acetylguaiacol		5.8	7.2	4.9
3-Methylcatechol		2.2	9.1	25.3
2-Acetoxyacetophenone		0.3	0.9	0.0
2,6-Dimethoxyphenol		4.7	8.0	0.5

3. Materials and Methods

3.1. Chemicals and Reagents

Tetrapropylammonium hydroxide (TPAOH; 25 wt% in water), RuCl₃·xH₂O (Ru, 36.0–40.0%), and dealkaline lignin were obtained from Macklin Biochemical Co., Ltd.. Sodium citrate dihydrate (99.0%), tetraethyl orthosilicate (>99%), bibenzyl ether (95.0%), phenol (99.0%), anisole (99.0%), diphenyl ether (≥99.9%), benzyl methyl ether (99.0%), ethyl acetate (99.5%), 3-phenoxytoluene (98.0%), and dodecane (>99.0%) were got from Aladdin Biochemical Technology Co., Ltd. Ni(NO₃)₂·6H₂O was obtained from Oukai Chemical Co., Ltd., benzyl phenyl ether (98.0%) from Energy Chemicals Co. Ltd., and di-p-tolyl ether (99.0%) from Alfa Chemical Co., Ltd.

3.2. Synthesis of S-1 and Macroporous S-1

S-1 and macroporous S-1 were prepared using a previously reported procedure with slight modifications [24]. In brief, tetraethyl orthosilicate was vigorously mixed with TPAOH (with a molar composition of 1 SiO₂:0.2 TPAOH:37 H₂O) until the formation of a clear solution. Afterward, the solution was heated in a 100 mL polytetrafluoroethylene-lined autoclave at 453 K for 3 days. After cooling to ~300 K, the solid precipitate was centrifuged and washed, then dried at 383 K, followed by calcination at 823 K to remove the templates. Finally, a white powdered product (S-1) was obtained.

Then, S-1 (0.4 g) was added to 4 mL of alkaline solution (TPAOH + NaCl) and heated in a polytetrafluoroethylene-lined steel autoclave at 453 K while stirring for 3–5 days. The solid was obtained by filtration, thoroughly washed, and then dried at 383 K. Finally, the resulting product was calcined at 823 K for 6 h to obtain macroporous S-1_x, where x denotes recrystallization time. For example, “S-1₅” indicates that the macroporous S-1 was synthesized by recrystallization of solid S-1 at 453 K for 5 days.

3.3. Preparation of Catalysts

In brief, S-1 zeolite or macroporous S-1 was impregnated with a solution of NaH₂PO₂, RuCl₃·xH₂O, NiCl₂·6H₂O, and sodium citrate, then pyrolyzed at 773 K under a vacuum after drying at 383 K. Finally, the catalysts were passivated in N₂ at room temperature. For each catalyst, the molar ratios of nP/nM (M = Ru and/or Ni) and nNi/nRu were 6/1 and the total load was 10 wt%.

3.4. Characterization of Catalysts and Supports

X-ray diffraction patterns were obtained with a SmartLab SE instrument. X-ray photoelectron spectra were obtained using an ESCALAB instrument. Energy-dispersive X-ray spectroscopy and transmission electron microscopy (TEM) images were obtained using a Tecnai™ G2 F20 transmission electron microscope.

3.5. Hydrogenolysis of Model Compounds

In a typical hydrogenolysis reaction, fresh catalyst (0.003 g), a model compound (0.2 mmol), and water (5 mL) were put into a reactor, which was then charged with 0.4 MPa N₂ and 0.6 MPa H₂ after exclusion of air. Reactions were conducted at 250 °C for a predetermined time while vigorously stirring. The reaction was terminated by cooling the reactor to ambient temperature using ice water. Ethyl acetate was used to retrieve the organic products from the reaction mixture. Quantitative analysis of the organic products was performed on a GC-FID employing *n*-dodecane as an internal standard. The hydrogenolysis conversion rate and product yield were calculated using the following equations.

$$\text{Conversion of reactant\%} = \frac{\text{moles of reactant reacted}}{\text{moles of reactant supplied}} \times 100 \quad (1)$$

$$\text{Yield of product (x)\%} = \frac{\text{moles of C atoms in product (x)}}{\text{moles of C atoms in reactant}} \times 100 \quad (2)$$

3.6. Hydrogenolysis of Lignin

Rather severe reaction conditions were employed due to the less depolymerization reactivity of lignin than model compounds. Typically, the catalyst (0.1 g), dealkaline lignin (0.1 g), and water (5 mL) were put into a reactor, which was sequentially charged with 10 bar H₂ after exclusion of air with H₂. Thereafter, the reaction was conducted at 280 °C for 3–12 h with vigorous stirring. After termination of the reaction, the hydrogenolysis products were retrieved with ethyl acetate. The liquid products in the aqueous and organic phases were analyzed quantitatively by HPLC-TQMS with the external standard method. The corresponding residues were characterized by two-dimensional nuclear magnetic resonance heteronuclear single quantum coherence (2D-NMR-HSQC) spectroscopy.

4. Conclusions

In this study, a macroporous S-1 array-supported Ru-Ni metallic phosphide composite was fabricated and introduced for the hydrogenolysis of lignin and C–O linkages containing lignin-related compounds. The unreduced Ru species-originated Lewis acid sites and the geometrical structure of the macroporous support significantly influenced the hydrogenolysis conversion rate and product selectivity. Notably, both the aryl ether and aliphatic ether linkages favor direct hydrogenation in the initiation reaction over Ru-Ni₁₂P₅/S-1₅. Furthermore, 2D-HSQC-NMR spectroscopy demonstrated that Ru-Ni₁₂P₅/S-1₅ efficiently depolymerized the C–O linkages of lignin. Different higher value-added products suitable for pharmaceutical production can be obtained by facilely tuning the reaction conditions.

Author Contributions: Conceptualization, B.C. and Z.-J.D.; methodology, Z.-Z.C. and B.C.; validation, Z.-Z.C. and L.-Q.H.; formal analysis, H.Y. and J.-M.H.; investigation, Z.-Z.C.; resources, Z.-Z.C. and B.C.; data curation, Z.-Z.C. and S.-J.Z.; writing—original draft preparation, Z.-Z.C.; writing—review and editing, B.C. and Z.-J.D.; supervision, B.C. and Z.-J.D.; project administration, B.C. and Z.-J.D.; funding acquisition, B.C. and Z.-J.D. All authors have read and agreed to the published version of the manuscript.

Funding: This research work was supported by the Fund from National Natural Science Foundation of China (Grant 21875186), Natural Science Basic Research Plan in Shaanxi Province of China (Grant 2019JM-259), Foundation of State Key Laboratory of High-efficiency Utilization of Coal and Green Chemical Engineering (Grant 2019-KF-17), China Postdoctoral Science Foundation (Grant 2017M623205) and Special Research Foundation of Education Bureau of Shaanxi Province (Grant 15JK1692).

Data Availability Statement: Not applicable.

Conflicts of Interest: The authors declare no conflict of interest.

References

1. Alonso, D.M.; Wettstein, S.G.; Dumesic, J.A. Bimetallic catalysts for upgrading of biomass to fuels and chemicals. *Chem. Soc. Rev.* **2012**, *41*, 8075–8898. [[CrossRef](#)] [[PubMed](#)]
2. Sahoo, A.; Saini, K.; Jindal, M.; Bhaskar, T.; Pant, K.K. Co-hydrothermal liquefaction of algal and lignocellulosic biomass: Status and perspectives. *Bioresour. Technol.* **2021**, *342*, 125948. [[CrossRef](#)] [[PubMed](#)]
3. Mohan, D.; Pittman, C.U.; Steele, P.H. Pyrolysis of wood/biomass for bio-oil: A critical review. *Energy Fuels* **2006**, *20*, 848–889. [[CrossRef](#)]
4. Wang, H.; Male, J.; Wang, Y. Recent advances in hydrotreating of pyrolysis bio-oil and its oxygen-containing model compounds. *ACS Catal.* **2013**, *3*, 1047–1070. [[CrossRef](#)]
5. Tuck, C.O.; Pérez, E.; Horváth, I.; Sheldon, R.; Poliakoff, M. Valorization of biomass: Deriving more value from waste. *Science* **2012**, *337*, 695–699. [[CrossRef](#)]
6. Zhao, M.X.; Wei, X.Y.; Qu, M.; Kong, J.; Li, Z.K.; Liu, J.; Zong, Z.M. Complete hydrocracking of dibenzyl ether over a solid acid under mild conditions. *Fuel* **2016**, *183*, 531–536. [[CrossRef](#)]
7. Luo, H.; Wang, L.; Li, G.; Shang, S.; Lv, Y.; Niu, J.; Gao, S. Nitrogen-doped carbon-modified cobalt-nanoparticle-catalyzed oxidative cleavage of lignin β -O-4 model compounds under mild conditions. *ACS Sustain. Chem. Eng.* **2018**, *6*, 14188–14196. [[CrossRef](#)]
8. Toor, S.S.; Reddy, H.; Deng, S.; Hoffmann, J.; Spangsmark, D.; Madsen, L.B.; Holm-Nielsen, J.B.; Rosendahl, L.A. Hydrothermal liquefaction of *Spirulina* and *nannochloropsis salina* under subcritical and supercritical water conditions. *Bioresour. Technol.* **2013**, *131*, 413–419. [[CrossRef](#)]
9. Liu, L.; Zhao, C.; Zheng, F.; Deng, D.; Anderson, M.A. Three-dimensional electrode design with conductive fibers and ordered macropores for enhanced capacitive deionization performance. *Desalination* **2021**, *498*, 114794. [[CrossRef](#)]
10. Mei, X.; Xiong, J.; Wei, Y.; Zhang, Y.; Zhang, P.; Yu, Q.; Zhao, Z.; Liu, J. High-efficient non-noble metal catalysts of 3D ordered macroporous perovskite-type La₂NiB'O₆ for soot combustion: Insight into the synergistic effect of binary Ni and B' sites. *Appl. Catal. B Environ.* **2020**, *275*, 119108. [[CrossRef](#)]
11. Zhang, P.; Mei, X.; Zhao, X.; Xiong, J.; Li, Y.; Zhao, Z.; Wei, Y. Boosting catalytic purification of soot particles over double Perovskite-Type La_{2-x}K_xNiCoO₆ catalysts with an ordered macroporous structure. *Environ. Sci. Technol.* **2021**, *55*, 11245–11254. [[CrossRef](#)] [[PubMed](#)]
12. Luo, Z.; Kong, J.; Ma, B.; Wang, Z.; Huang, J.; Zhao, C. Liquefaction and hydrodeoxygenation of polymeric lignin using a hierarchical Ni microreactor catalyst. *ACS Sustain. Chem. Eng.* **2020**, *8*, 2158–2166. [[CrossRef](#)]

13. Golubeva, M.A.; Zakharyan, E.M.; Maximov, A.L. Transition metal phosphides (Ni, Co, Mo, W) for hydrodeoxygenation of biorefinery products (a review). *Pet. Chem.* **2020**, *60*, 1109–1128. [[CrossRef](#)]
14. Li, H.; Li, G. Enhancing activity of Ni₂P-based catalysts by a Yolk–Shell structure and transition metal-doping for catalytic transfer hydrogenation of vanillin. *Energy Fuels* **2021**, *35*, 4158–4168. [[CrossRef](#)]
15. Zhao, H.Y.; Li, D.; Bui, P.; Oyama, S.T. Hydrodeoxygenation of guaiacol as model compound for pyrolysis oil on transition metal phosphide hydroprocessing catalysts. *Appl. Catal. A Gen.* **2011**, *391*, 305–310. [[CrossRef](#)]
16. García-Pérez, D.; Alvarez-Galvan, M.C.; Capel-Sanchez, M.C.; Blanco-Brieva, G.; Morales-delaRosa, S.; Campos-Martin, J.M.; Fierro, J.L.G. Influence of bimetallic characteristics on the performance of MoCoP and MoFeP catalysts for methyl laurate hydrodeoxygenation. *Catal. Today* **2021**, *367*, 43–50. [[CrossRef](#)]
17. Bonita, Y.; O’Connell, T.P.; Miller, H.E.; Hicks, J.C. Revealing the hydrogenation performance of RuMo phosphide for chemoselective reduction of functionalized aromatic hydrocarbons. *Ind. Eng. Chem. Res.* **2019**, *58*, 3650–3658. [[CrossRef](#)]
18. Bonita, Y.; Jain, V.; Geng, F.; O’Connell, T.P.; Wilson, W.N.; Rai, N.; Hicks, J.C. Direct synthesis of furfuryl alcohol from furfural: Catalytic performance of monometallic and bimetallic Mo and Ru phosphides. *Catal. Sci. Technol.* **2019**, *9*, 3656–3668. [[CrossRef](#)]
19. Charisiou, N.D.; Siakavelas, G.I.; Papageridis, K.N.; Motta, D.; Dimitratos, N.; Sebastian, V.; Polychronopoulou, K.; Goula, M.A. The effect of noble metal (M: Ir, Pt, Pd) on M/Ce₂O₃-γ-Al₂O₃ catalysts for hydrogen production via the steam reforming of glycerol. *Catalysts* **2020**, *10*, 790. [[CrossRef](#)]
20. Gao, K.; Sahraei, O.A.; Iliuta, M.C. Development of residue coal fly ash supported nickel catalyst for H₂ production via glycerol steam reforming. *Appl. Catal. B-Environ.* **2021**, *298*, 119958. [[CrossRef](#)]
21. Ma, Y.X.; Ma, Y.Y.; Li, J.J.; Ye, Z.M.; Hu, X.; Dong, D.H. Electrospun nanofibrous Ni/LaAlO₃ catalysts for syngas production by high temperature methane partial oxidation. *Int. J. Hydrogen Energy* **2022**, *47*, 3867–3875. [[CrossRef](#)]
22. Charisiou, N.D.; Siakavelas, G.; Tzounis, L.; Sebastian, V.; Monzon, A.; Baker, M.A.; Hinder, S.J.; Polychronopoulou, K.; Yentekakis, I.V.; Goula, M.A. An in depth investigation of deactivation through carbon formation during the biogas dry reforming reaction for Ni supported on modified with CeO₂ and La₂O₃ zirconia catalysts. *Int. J. Hydrogen Energy* **2018**, *43*, 18955–18976. [[CrossRef](#)]
23. Yang, X.Y.; Tian, G.; Chen, L.H.; Li, Y.; Rooke, J.C.; Wei, Y.X.; Liu, Z.M.; Deng, Z.; Tendeloo, G.V.; Su, B.L. Well-organized zeolite nanocrystal aggregates with interconnected hierarchically micro–meso–macropore systems showing enhanced catalytic performance. *Chem. A Eur. J.* **2011**, *17*, 14987–14995. [[CrossRef](#)]
24. Dai, C.; Zhang, A.; Li, L.; Hou, H.; Ding, F.; Li, J.; Mu, D.; Song, C.; Liu, M.; Guo, X. Synthesis of hollow nanocubes and macroporous monoliths of silicalite-1 by alkaline treatment. *Chem. Mater.* **2013**, *25*, 4197–4205. [[CrossRef](#)]
25. Larsson, E. An x-ray investigation of the Ni-P system and the crystal structures of NiP and NiP₂. *Arkiv Kemi* **1965**, *23*, 335–365.
26. Diao, Z.J.; Huang, L.Q.; Chen, B.; Gao, T.; Cao, Z.Z.; Ren, X.D.; Zhao, S.J.; Li, S. Amorphous Ni-Ru bimetallic phosphide composites as efficient catalysts for the hydrogenolysis of diphenyl ether and lignin. *Fuel* **2022**, *324*, 124489. [[CrossRef](#)]
27. Wang, S.; Hu, J.; Gui, X.; Lin, S.; Tu, Y. RuO₂ active particles supported on Ni₁₂P₅ as excellent electrocatalysts for LiO₂ batteries. *Solid State Ionics* **2021**, *372*, 115773. [[CrossRef](#)]
28. Wang, Y.; Qiao, M.; Li, Y.; Wang, S. Tuning surface electronic configuration of NiFe LDHs nanosheets by introducing cation vacancies (Fe or Ni) as highly efficient electrocatalysts for oxygen evolution reaction. *Small* **2018**, *14*, 1800136. [[CrossRef](#)]
29. Morgan, D.J. Resolving ruthenium: XPS studies of common ruthenium materials. *Surf. Interface Anal.* **2015**, *47*, 1072–1079. [[CrossRef](#)]
30. Topalian, P.J.; Carrillo, B.A.; Cochran, P.M.; Takemura, M.F.; Bussell, M.E. Synthesis and hydrodesulfurization properties of silica-supported nickel-ruthenium phosphide catalysts. *J. Catal.* **2021**, *403*, 173–180. [[CrossRef](#)]
31. Huang, L.-Q.; Diao, Z.-J.; Chen, B.; Du, Q.-P.; Duan, K.-Y.; Zhao, S.-J. Hydrogenolysis of lignin and C–O linkages containing lignin-related compounds over an amorphous CoRuP/SiO₂ catalyst. *Catalysts* **2022**, *12*, 1328. [[CrossRef](#)]
32. Wang, Y.; Chen, M.; Shi, J.; Zhang, J.; Li, C.; Wang, J. Catalytic depolymerization of kraft lignin for liquid fuels and phenolic monomers over molybdenum-based catalysts: The effect of supports. *J. Fuel Chem. Technol.* **2021**, *49*, 1922–1934. [[CrossRef](#)]
33. Rolison, D.R. Catalytic nanoarchitectures—The importance of nothing and the unimportance of periodicity. *Science* **2003**, *299*, 1698–1701. [[CrossRef](#)]
34. Wang, A.; Shi, Y.; Yang, L.; Fan, G.; Li, F. Ordered macroporous Co₃O₄-supported Ru nanoparticles: A robust catalyst for efficient hydrodeoxygenation of anisole. *Catal. Commun.* **2021**, *153*, 106302. [[CrossRef](#)]
35. Yang, P.; Zhou, S.; Du, Y.; Li, J.; Lei, J. Synthesis of ordered meso/macroporous H₃PW₁₂O₄₀/SiO₂ and its catalytic performance in oxidative desulfurization. *RSC Adv.* **2016**, *6*, 53860–53866. [[CrossRef](#)]
36. Molinari, V.; Giordano, C.; Antonietti, M.; Esposito, D. Titanium nitride-nickel nanocomposite as heterogeneous catalyst for the hydrogenolysis of aryl ethers. *J. Am. Chem. Soc.* **2014**, *136*, 1758–1761. [[CrossRef](#)]
37. Yu, Z.; Wang, A.; Liu, S.; Yao, Y.; Sun, Z.; Li, X.; Liu, Y.; Wang, Y.; Camaioni, D.M.; Lercher, J.A. Hydrodeoxygenation of phenolic compounds to cycloalkanes over supported nickel phosphides. *Catal. Today* **2019**, *319*, 48–56. [[CrossRef](#)]
38. Gutiérrez-Rubio, S.; Berenguer, A.; Přeč, J.; Opanasenko, M.; Ochoa-Hernández, C.; Pizarro, P.; Čejka, J.; Serrano, D.P.; Coronado, J.M.; Moreno, I. Guaiacol hydrodeoxygenation over Ni₂P supported on 2D-zeolites. *Catal. Today* **2020**, *345*, 48–58. [[CrossRef](#)]
39. Nelson, R.C.; Baek, B.; Ruiz, P.; Goundie, B.; Brooks, A.; Wheeler, M.C.; Frederick, B.G.; Grabow, L.C.; Austin, R.N. Experimental and theoretical insights into the hydrogen-efficient direct hydrodeoxygenation mechanism of phenol over Ru/TiO₂. *ACS Catal.* **2015**, *5*, 6509–6523. [[CrossRef](#)]

40. Li, K.; Wang, R.; Chen, J. Hydrodeoxygenation of anisole over silica-supported Ni₂P, MoP, and NiMoP catalysts. *Energy Fuels* **2011**, *25*, 854–863. [[CrossRef](#)]
41. Shi, Y.; Zhang, B. Recent advances in transition metal phosphide nanomaterials: Synthesis and applications in hydrogen evolution reaction. *Chem. Soc. Rev.* **2016**, *45*, 1529–1541. [[CrossRef](#)] [[PubMed](#)]
42. Rodríguez-Aguado, E.; Rodríguez-Aguado, A.; Cecilia, J.A.; Ballesteros-Plata, D.; López-Olmo, R.; Rodríguez-Castellón, E. Co_xP_y catalysts in HDO of phenol and dibenzofuran: Effect of P content. *Top. Catal.* **2017**, *60*, 1094–1107. [[CrossRef](#)]
43. Cecilia, J.A.; Infantes-Molina, A.; Sanmartín-Donoso, J.; Rodríguez-Aguado, E.; Ballesteros-Plata, D.; Rodríguez-Castellón, E. Enhanced HDO activity of Ni₂P promoted with noble metals. *Catal. Sci. Technol.* **2016**, *6*, 7323–7333. [[CrossRef](#)]
44. Galindo-Ortega, Y.L.; Infantes-Molina, A.; Huirache-Acuña, R.; Barroso-Martín, I.; Rodríguez-Castellón, E.; Fuentes, S.; Alonso-Nuñez, G.; Zepeda, T.A. Active ruthenium phosphide as selective sulfur removal catalyst of gasoline model compounds. *Fuel Process. Technol.* **2020**, *208*, 106507. [[CrossRef](#)]
45. Zhao, C.; Lercher, J.A. Upgrading pyrolysis oil over Ni/HZSM-5 by cascade reactions. *Angew. Chem. Int. Ed.* **2012**, *51*, 5935–5940. [[CrossRef](#)]
46. Sergeev, A.G.; Hartwig, J.F. Selective, nickel-catalyzed hydrogenolysis of aryl ethers. *Science* **2011**, *332*, 439–443. [[CrossRef](#)]
47. Luo, Y.R. *Handbook of Bond Dissociation Energies in Organic Compounds*; CRC: New York, NY, USA, 2003.
48. Si, X.; Chen, J.; Lu, F.; Liu, X.; Ren, Y.; Lu, R.; Jiang, H.; Liu, H.; Miao, S.; Zhu, Y.; et al. Immobilized Ni clusters in mesoporous aluminum silica nanospheres for catalytic hydrogenolysis of lignin. *ACS Sustain. Chem. Eng.* **2019**, *7*, 19034–19041. [[CrossRef](#)]
49. Kong, J.; Li, L.; Zeng, Q.; Long, J.; He, H.; Wang, Y.; Liu, S.; Li, X. Production of 4-Ethylphenol from lignin depolymerization in a novel Surfactant-Free Microemulsion reactor. *Ind. Eng. Chem. Res.* **2021**, *60*, 17897–17906. [[CrossRef](#)]
50. Amiri, M.T.; Bertella, S.; Questell-Santiago, Y.M.; Luterbacher, J.S. Establishing lignin structure-upgradeability relationships using quantitative 1H–13C heteronuclear single quantum coherence nuclear magnetic resonance (HSQC-NMR) spectroscopy. *Chem. Sci.* **2019**, *10*, 8135–8142. [[CrossRef](#)]
51. Wang, X.B.; Du, L.D.; Wang, S.M.; Du, G.H. Vanillin. In *Natural Small Molecule Drugs from Plants*; Springer: Singapore, 2018; pp. 343–346.
52. Applová, L.; Karličková, J.; Warncke, P.; Macáková, K.; Hrubša, M.; Macháček, M.; Tvrđý, V.; Fischer, D.; Mladěnka, P. 4-Methylcatechol, a flavonoid metabolite with potent antiplatelet effects. *Mol. Nutr. Food Res.* **2019**, *63*, 1900261. [[CrossRef](#)]
53. Morita, K.; Arimochi, H.; Ohnishi, Y. In vitro cytotoxicity of 4-Methylcatechol in murine tumor cells: Induction of apoptotic cell death by extracellular pro-oxidant action. *J. Pharmacol. Exp. Ther.* **2003**, *306*, 317–323. [[CrossRef](#)] [[PubMed](#)]